Chemical Engineering Journal 404 (2021) 127124

Contents lists available at ScienceDirect

Chemical Engineering Journal

journal homepage: www.elsevier.com/locate/cej

Interface engineering of Co_3Fe_7-Fe_3C heterostructure as an efficient oxygen reduction reaction electrocatalyst for aluminum-air batteries

Min Jiang, Chaopeng Fu *, Ruiqi Cheng, Tongyao Liu, Meilin Guo, Pengyu Meng, Jiao Zhang, Baode Sun

School of Materials Science and Engineering, Shanghai Jiao Tong University, Shanghai 200240, PR China

ARTICLE INFO

Keywords:
Co_3Fe_7-Fe_3C heterostructure
Electrocatalyst
Oxygen reduction
Al-air battery

ABSTRACT

Aluminum-air batteries with merits of high theoretical energy densities, low cost and environmental-friendliness are promising candidates for next-generation energy storage and conversion systems. Rational design of efficient heterogeneous catalysts for oxygen reduction reaction (ORR) in neutral and alkaline solutions is of great significance for aluminum-air batteries. Herein, an interface engineering strategy is proposed to realize Co_3Fe_7-Fe_3C heterostructure with abundant interfaces anchored on 3D honeycomb-like N-doped carbon, which inherits the original structure of the biomass precursor. The as-prepared Co_3Fe_7-Fe_3C heterostructure on honeycomb-like N-doped carbon (denoted as Co_3Fe_7-Fe_3C/HNC) displays remarkable electrocatalytic activity and stability towards ORR in both alkaline and neutral solutions. It shows a very positive onset potential of 0.98 V and a half-wave potential of 0.90 V in 0.1 M KOH solution (E_{onset} = 0.78 V and $E_{1/2}$ = 0.64 V in 3.5% NaCl solution) towards ORR. The high ORR performance is mainly ascribed to the abundant engineered interfaces, which can not only boost the intrinsic activity, but also guarantee fast charge transfer. The superior ORR performance is also supported by the density functional theory calculation. Moreover, the fabricated Al-air battery displays a larger working voltage and a higher power density compared with those of Pt/C. Furthermore, the Co_3Fe_7-Fe_3C/HNC catalyst exhibits outstanding stability and durability during mechanical recharging and continuous discharging processes. This work demonstrates a new strategy to design and construct multifunctional catalysts with interfacial structure for high performance metal-air batteries.

1. Introduction

The increasing energy crisis and environmental deterioration due to the impending depletion of fossil fuels have stimulated considerable efforts to explore clean and sustainable energy sources [1,2]. Among various energy storage and conversion technologies, Aluminum-air (Al-air) batteries demonstrate promising potential due to the high theoretical energy density (2800 Wh kg^{-1}), low cost, good environmental benignity and safe operation [3,4]. However, the power densities of Al-air batteries are limited by sluggish oxygen reduction reaction (ORR) kinetics at air cathodes, which hinders commercial implementation of Al-air batteries. Pt-based noble metal materials are well known as effective electrocatalysts to accelerate ORR [5,6]. However, the reserve scarcity, high cost and unsatisfied stability of Pt severely hinder their large-scale commercialization [7]. Therefore, it is urgent to design and develop high performance and cost-effective alternative nonprecious metal-based catalysts for ORR [8].

In the past decades, tremendous efforts have been devoted to exploring transition metal-based catalysts for ORR, such as nanosized transition metals [7,9], transition metal compounds (oxides [10], nitrides [11], and carbides [12]) and transition metal alloys [13–15] with the characteristics of low cost, abundant resources and relatively satisfactory activity. Despite the considerable efforts are devoted, the oxygen reduction performance of these catalysts still needs to be improved. Generally, an ideal ORR electrocatalyst should have optimal well-balanced adsorption energy to achieve good performance [16,17]. Tuning chemical composition is an efficient strategy to modulate adsorption–desorption abilities of intermediates during ORR. Compared with a single component, composite catalysts with specifically designed interfaces can tune adsorption–desorption energies of oxygen intermediates, thus enhance the intrinsically catalytic activity for ORR [16,18]. This is mainly ascribed to the interfacial effects caused by the

* Corresponding author.
E-mail address: chaopengfu@sjtu.edu.cn (C. Fu).

https://doi.org/10.1016/j.cej.2020.127124
Received 12 July 2020; Received in revised form 11 September 2020; Accepted 19 September 2020
Available online 23 September 2020

created interface between different components, and the interface can enhance ORR performance by accelerating electron transfer, stabilizing catalysts and optimizing adsorption/desorption energies of active species [19–24]. Recently, Diao and co-workers demonstrated that the tungsten nitride/tungsten carbide heterostructure electrocatalyst could facilitate ORR through fast charge transfer from WC to W_2N [25]. The interface at $NiSe_2/CoSe_2$ heterostructure was also proved to boost electrochemical performance for ORR [26]. Therefore, the construction of appropriate heterostructure may represent an effective way to enhance electrocatalytic ORR performance.

Iron carbides have recently received intensive attention as promising candidates for ORR due to the high corrosion resistance, high activity, and good chemical stability [27–29]. Co_xFe_y bimetallic-based materials have also been developed as efficient electrocatalysts for ORR owning to their high activity and good durability [7,9]. Thus, it is anticipated that controllable regulation of interfacial structure between Co_xFe_y and Fe_3C can not only combine the merits of Co_xFe_y and Fe_3C, but also accelerate charge transfer from the heterostructure, thus possibly meeting practical demands for Al-air batteries.

Herein, a green and low-cost strategy is developed to facilely construct Co_3Fe_7-Fe_3C heterostructure with interface anchored on biomass derived 3D honeycomb-like N-doped carbon (denoted as Co_3Fe_7-Fe_3C/HNC) for ORR. The synthesized Co_3Fe_7-Fe_3C/HNC displays remarkable activity and stability toward ORR with an onset potential of 0.98 V and a half-wave potential of 0.90 V in O_2-saturated 0.1 M KOH solution (E_{onset} = 0.78 V and $E_{1/2}$ = 0.64 V in NaCl solution), which are more positive than those on benchmark Pt/C. Alkaline and neutral Al–air batteries are assembled based on Co_3Fe_7-Fe_3C/HNC air-cathode, and they exhibit high power densities and large working voltages, outperforming the commercial Pt/C catalyst. This work provides a new thought into the construction of heterostructure for designing highly efficient and low-cost catalysts for metal-air batteries.

2. Experimental sections

2.1. Preparations of Co_3Fe_7-Fe_3C/HNC, Fe_3C/HNC and Co_3Fe_7/HNC

Biomass waste, soybean roots were firstly thoroughly washed with ethanol and water several times and dried at 80 °C in an oven. The dry soybean root powder (0.50 g) and K_2FeO_4 (0.22 g) were dispersed in water (50 mL), and the mixture was heated to 60 °C and stirred for 6 h to complete the pre-oxidation. Then 0.05 g of $Co(NO_3)_2{\cdot}6H_2O$ and 0.5 g of melamine were slowly added to the above solution with continuous stirring for another 1 h. Subsequently, the obtained mixture was placed into liquid nitrogen to ensure a quick freeze followed by freeze drying overnight. After that, the powder was annealed at 900 °C for 2 h in a tubular furnace under N_2 flow. The Co/HNC, Fe_3C/HNC, Co_3Fe_7/HNC and HNC were also synthesized with the similar procedure via adjusting the ratio of Fe to Co.

The dry soybean root powder (0.50 g) and K_2FeO_4 (0.22 g) were dispersed in water (50 mL), and the mixture was heated to 60 °C and stirred for 6 h to complete the pre-oxidation. Then 0.1 g of Co $(NO_3)_2{\cdot}6H_2O$ and 0.5 g of melamine were added to the above solution. Subsequently, the mixture was placed into liquid nitrogen to ensure a quick freeze followed by freeze drying overnight. After that, the powder was annealed at 900 °C for 2 h under N_2 flow to obtain Co_3Fe_7/HNC. Fe_3C/HNC was also synthesized via the identical process without adding $Co(NO_3)_2{\cdot}6H_2O$.

2.2. Characterizations

Morphology and microstructure of the samples were characterized by Field-emission scanning electron microscope (FE-SEM, MIRA3 LHM, TESCAN) and transmission electron microscopy (FE-TEM, TALOS F200X, FEI) equipped with elemental mapping at an accelerating voltage of 5 kV and 200 kV, respectively. Powder X-ray diffraction (XRD) measurements were performed on a Rigaku Ultima IV diffractometer using Cu Kα radiation (λ = 0.15418 nm) with a scanning speed of 2° min^{-1}. X-ray photoelectron spectroscopy (XPS) was carried out on an Axis Ultra DLD with Al Kα radiation of 1486.6 eV as the excitation source. Brunauer-Emmett-Teller (BET) measurement was carried out using Quantachrome Autosorb iQ3 instrument at 77 K. Prior to nitrogen physisorption, all samples were degassed at 300 °C for 4 h under vacuum. All Raman spectra were obtained on an inVia Qontor confocal Raman microscope (Renishaw) using a 532 nm laser.

2.3. Electrochemical measurements

Electrochemical measurements were conducted in both alkaline and neutral solutions on Gamry REF 600 equipped with a rotating ring-disk electrode system (PINE, USA). Each measurement was performed with a typical three-electrode configuration using glassy carbon rotating ring disk electrode (GC-RRDE, 5 mm in diameter, PEEK, PINE Instrument Inc.) modified by a thin catalyst film as working electrode, graphite electrode as counter electrode and saturated calomel electrode (SCE) as reference electrode. The GC electrode was polished with alumina powder (0.05 μm) felt polishing pads and then sonicated in deionized water and ethanol successively. Catalyst ink was prepared by ultrasonically dispersing 3 mg of as-synthesized catalyst materials (Co_3Fe_7-Fe_3C/HNC, Co/HNC, Fe_3C/HNC, Co_3Fe_7/HNC, HNC and or 20 wt% Pt/C) in a suspension containing 240 μL of ethanol, 720 μL of water and 40 μL of 5% Nafion solution for 1 h to obtain a uniform dispersion ink (3 mg mL^{-1}). After that, 20 μL of the catalyst dispersion was loaded onto the surface of GC electrode followed by drying at room temperature naturally. The catalyst loading on RRDE was ~0.30 mg cm^{-2}. Prior to the electrochemical testing, the solution was bubbled with oxygen for 30 mins. Cyclic voltammetry (CV) and linear sweep voltammetry (LSV) were conducted in 0.1 M KOH alkaline solution or 3.5 wt% NaCl neutral solution. LSV curves were recorded at a rotation speed of 1600 rpm at a scan rate of 10 mV s^{-1} with a potential window ranging from 0.1 to −0.8 V (vs. SCE). All potentials in this work were referenced to the reversible hydrogen electrode (RHE) by the formula: $E_{RHE} = E_{SCE} + 0.059pH + 0.241$. RRDE measurements were also conducted by linear sweep voltammetry (LSV). All the obtained curves were corrected by the 95%-iR compensation. The following equations were used to calculate the number of electrons transferred (n) and yield of hydrogen peroxide.

$$\%(H_2O_2) = 200 \times \frac{I_r/N}{I_d + I_r/N} \quad (1)$$

$$n = 4 \times \frac{I_d}{I_d + I_r/N} \quad (2)$$

where I_d is the Faradaic current at the disk, I_r is the Faradaic current and N is the H_2O_2 collection efficiency (0.34) determined from the reduction of $K_3Fe[CN]_6$.

2.4. Calculations details

The computational calculations were carried out using the density functional theory (DFT) utilizing the Cambridge sequential total energy Package (CASTEP) package [30,31]. Details are shown in supporting information.

2.5. Al-air battery measurements

For cathode preparation, electrocatalyst, carbon black (Vulcan XC-72) and poly(tetrafluoroethylene) (PTFE) (60 wt% emulsion) with a mass ratio of 20:60:20 were mixed in ethanol and stirred to form to a film, which was then pressed on the gas diffusion layer and sintered at 300 °C for 10 min (≈2.5 mg cm^{-2}). The working area of the air cathode is 3.14 cm^2. The anode was home-made Al-Mg-Sn alloy plate, and the

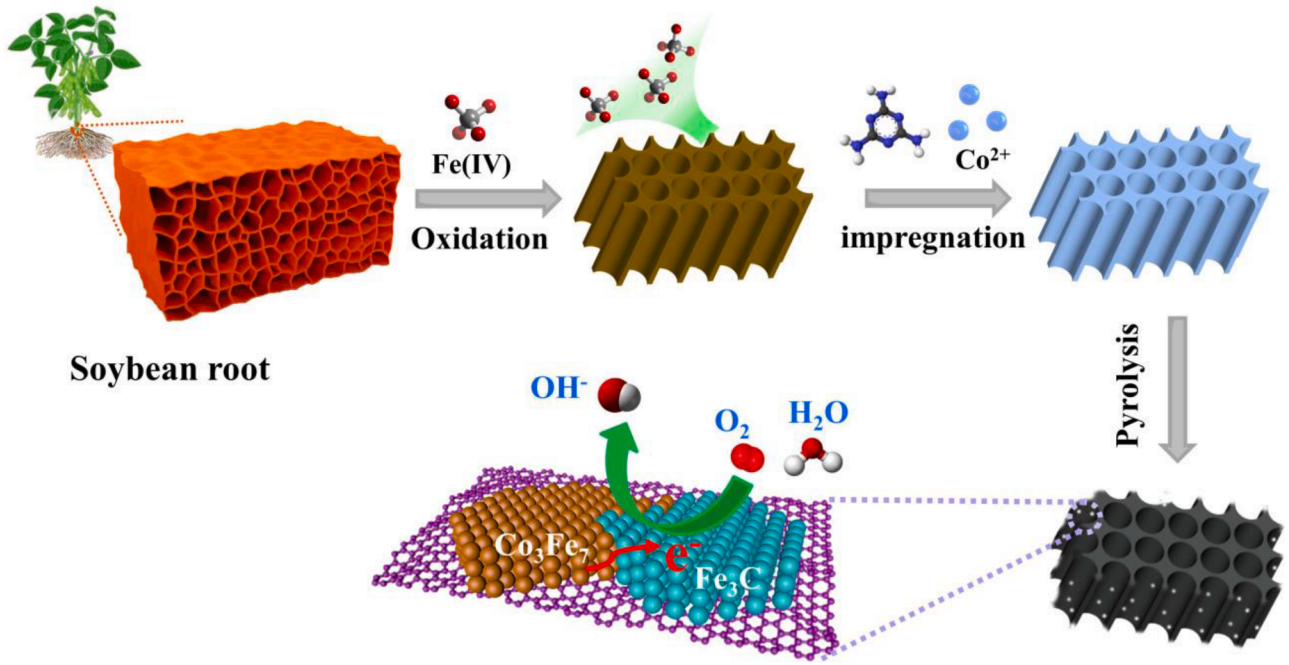

Fig. 1. Schematic illustration of the synthesis of Co_3Fe_7-Fe_3C/HNC.

electrolyte was either 4 M NaOH solution or 3.5 wt% NaCl solution.

3. Results and discussion

Fig. 1 illustrates the detailed preparation procedure of Co_3Fe_7-Fe_3C/HNC through a facile process including biomass oxidation and pyrolysis. Biomass soybean roots with a large amount of cellulose/hemicellulose microfibers and lignin and unique honeycomb-like microstructure were used as the main carbon source. Firstly, the soybean root powder was oxidized by a strong oxidant K_2FeO_4 in an aqueous solution. During this process, K_2FeO_4 not only acts as an iron precursor, but also acts as an oxidizing agent to break the cross-linking between lignocellulose, cellulose and hemicellulose, as these cellulose macromolecules hinder the formation of interfacial structure. Moreover, the soybean roots derived carbon can inherit the honeycomb-like structure [32], which provides fast ion transport channels and active sites for electrocatalytic reaction. The unique feature of soybean roots is beneficial to bind and immobilize metal ions and can provide suitable sites for regulating heterostructure with precisely controlled interface. Secondly, Co and N precursors were added in the above solution, and the *in-situ* generated iron species with the added cobalt ions were trapped by the soybean roots. Then the solution was freeze dried to obtain an aerogel to reduce the shrinkage or toughening of the material. Finally, the organic aerogel was pyrolyzed under N_2 flow to generate Co_3Fe_7-Fe_3C/HNC. The sample composition can be regulated by modulating an appropriate molar ratio of cobalt to iron. When there is no Co precursor, Fe_3C/HNC is obtained. When the ratio of Co to Fe is 0.25, the Co_3Fe_7-Fe_3C/HNC with interfacial structure is constructed. When the ratio of Co to Fe reaches 0.5, Co_3Fe_7/HNC is obtained.

To demonstrate the role of soybean root in the formation of Co_3Fe_7-Fe_3C heterostructure, soybean flour instead of soybean root was used as carbon precursor, and the obtained product was denoted as Co_3Fe_7/Fe_3C/NC. The X-ray diffraction (XRD) pattern confirms the formation of orthorhombic Fe_3C phase and cubic Co_3Fe_7 phase in Co_3Fe_7/Fe_3C/NC (Fig. S1), suggesting that the change of precursors does not change the crystal structure. The Co_3Fe_7/Fe_3C/NC displays disorder carbon structure without the formation of 3D honeycomb-like carbon (Fig. S2a-b), as there is no existence of naturally rich pores or multi-channels in soybean flour. Moreover, the TEM image of Co_3Fe_7/Fe_3C/NC displays that metal nanoparticles are anchored in graphitic carbon layers and there is no observed interface between Co_3Fe_7 and Fe_3C (Fig. S2c-d). The electrochemical performance of Co_3Fe_7/Fe_3C/NC is also far behind the designed product Co_3Fe_7-Fe_3C/HNC (Fig. S3). The above result shows that soybean roots play key roles in the construction of Co_3Fe_7-Fe_3C heterostructure architecture.

The samples with various ratios of Co to Fe were examined by X-ray diffraction (XRD). Fig. 2a represents the XRD patterns of HNC, Co_3Fe_7/HNC, Fe_3C/HNC and Co_3Fe_7-Fe_3C/HNC. As expected, the diffraction peak at ~26.5° is assigned to (0 0 2) crystal plane of graphitic carbon, verifying the formation of graphitic structure during the pyrolysis [33]. The residual peaks of Fe_3C/HNC and Co_3Fe_7/HNC are well assigned to orthorhombic Fe_3C phase (PDF No. 35-0772) and cubic Co_3Fe_7 phase (PDF No. 48-1816), respectively. Both Fe_3C and Co_3Fe_7 phases are observed in the XRD pattern of Co_3Fe_7-Fe_3C/HNC. In Fig. 2b, the Co_3Fe_7-Fe_3C/HNC displays a larger Brunauer–Emmett–Teller (BET) surface area of 743 $m^2\ g^{-1}$ than Fe_3C/HNC (498 $m^2\ g^{-1}$), Co_3Fe_7/HNC (393 $m^2\ g^{-1}$) and HNC (197 $m^2\ g^{-1}$), and the high specific surface area can facilitate ion transfer and expose a large number of active sites. The mesoporous structure of Co_3Fe_7-Fe_3C/HNC is identified by the typical type-IV profile with a distinct hysteresis loop, and the predominant pore size is ~3.8 nm with a total pore volume of 0.312 $cm^3\ g^{-1}$ (Fig. S4). Fig. 2c shows the Raman spectra of Co_3Fe_7-Fe_3C/HNC, Co_3Fe_7/HNC, Fe_3C/HNC and HNC, where two typical peaks at 1340 and 1568 cm^{-1} are assigned to the disordered carbon and graphitic carbon, respectively [34]. It is known that the higher value of I_G/I_D reveals higher graphitization degree and conductivity [35], and the ratio of I_G/I_D of Co_3Fe_7-Fe_3C/HNC, Co_3Fe_7/HNC, Fe_3C/HNC and HNC are 1.35, 1.26, 1.11 and 0.88, suggesting that the addition of Co and Fe can boost graphitization degree and reduce defect sites.

X-ray photoelectron spectroscopy (XPS) was introduced to investigate the chemical composition of Co_3Fe_7-Fe_3C/HNC. The long-range survey scan clearly exhibits the presence of C, N, Fe and Co in Co_3Fe_7-Fe_3C/HNC (Fig. S5). The corresponding contents of C, N, Fe, Co and O in Co_3Fe_7-Fe_3C/HNC are 80.6, 6.3, 6.4, 1.2 and 5.5 at%, respectively. The fitted C 1s XPS of Co_3Fe_7-Fe_3C/HNC is shown in Fig. S6, and the main peak located at 284.8 eV is attributed to the sp^2 carbon atoms in the form of conjugated honeycomb lattice [36]. The peak at 285.4 eV corresponds to C–C bond, confirming the partially graphitized structure in Co_3Fe_7-

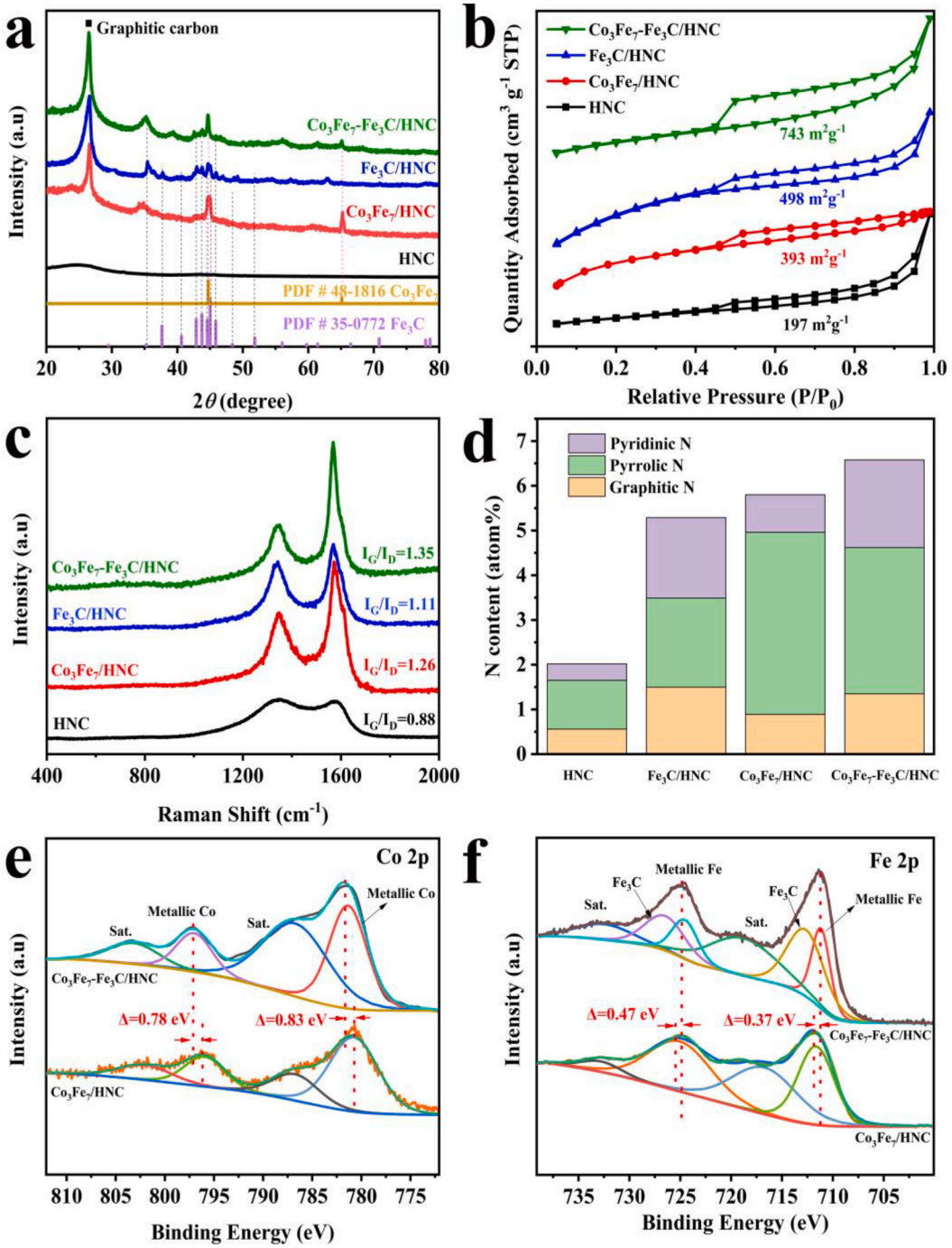

Fig. 2. (a) XRD patterns, (b) N_2 adsorption/desorption isotherms and (c) Raman spectra of HNC, Co_3Fe_7/HNC, Fe_3C/HNC and Co_3Fe_7-Fe_3C/HNC. (d) N contents of HNC, Co_3Fe_7/HNC, Fe_3C/HNC and Co_3Fe_7-Fe_3C/HNC. (e) Co 2p and (f) Fe 2p XPS of Co_3Fe_7/HNC and Co_3Fe_7-Fe_3C/HNC.

Fe_3C/HNC [37]. The peak at 287.2 eV is attributed to C-N bond, while the peak centered at 290.5 eV explains the existence of π–π* bond [38]. Besides, the deconvoluted N 1s XPS of Co_3Fe_7-Fe_3C/HNC shown in Fig. S7 reveals the presence of pyridinic N (398.6 eV), pyrrolic N (401.1 eV) and graphitic N (403.8 eV) [39], confirming the doping of N in the honeycomb-like carbon. The total N content in Co_3Fe_7-Fe_3C/HNC (6.29%) is higher than that of Co_3Fe_7/HNC (5.80%), Fe_3C/HNC (5.29%) and HNC (2.02%), suggesting that the addition of cobalt and iron can facilitate N doping (Fig. 2d). It is noticed that an excess addition of cobalt can reduce N content in the final product. Moreover, the Co_3Fe_7-Fe_3C/HNC possesses more pyridinic N and pyrrolic N, which can promote ORR electrocatalytic process [40]. The fitted Co 2p XPS of Co_3Fe_7-Fe_3C/HNC displaying peaks at 781.4 eV and 797.0 eV presents metallic Co in Co_3Fe_7 alloy (Fig. 2e), which is further confirmed by the satellite peaks at 786.7 eV and 803.2 eV [41]. Similarly, the Fe 2p XPS of Co_3Fe_7-Fe_3C/HNC deconvoluted to six peaks in Fig. 2f are ascribed to metallic Fe in Co_3Fe_7 alloy (711.2 eV and 724.5 eV), Fe_3C species (712.7 and 726.5 eV) and the satellite peaks (719.1 eV and 732.5 eV) [42,43]. Importantly, the Co $2p_{3/2}$ and Co $2p_{1/2}$ peaks in Co 2p spectrum of Co_3Fe_7-Fe_3C/HNC display positive shift compared to those of Co_3Fe_7/HNC (0.83 and 0.78 eV, respectively, Fig. 2e). Similarly, the Fe $2p_{3/2}$ and Fe $2p_{1/2}$ peaks of Co_3Fe_7-Fe_3C/HNC display negative shift compared to those of Co_3Fe_7/HNC (0.37 and 0.47 eV, respectively, Fig. 2f). The result strongly suggests there is strong electronic interaction between Fe_3C and

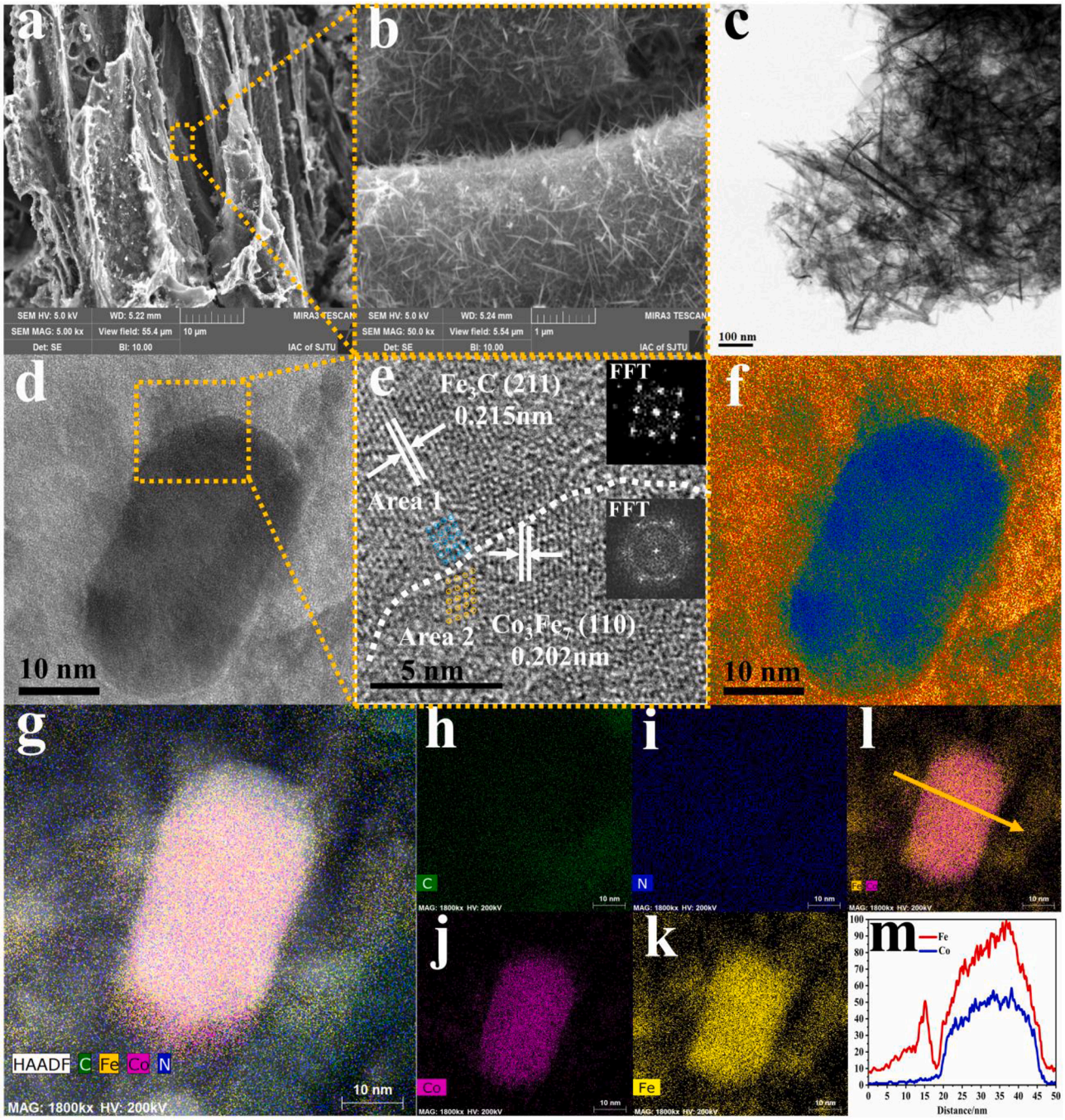

Fig. 3. (a, b) Typical SEM images and TEM images (c) of Co_3Fe_7-Fe_3C/HNC heterostructure. (d, e) High-magnification TEM images of Co_3Fe_7-Fe_3C/HNC. Inset: FFT pattern of Co_3Fe_7 and Fe_3C. (f) Colored intensity image of the two phases interfaces structure with Co_3Fe_7 and Fe_3C. (g–k) HAADF-STEM images with elemental mapping of C, N, Co, and Fe. (l, m) The corresponding EDS line-scan spectra.

Co_3Fe_7 in the heterostructure. The electron transfer from Co_3Fe_7 to Fe_3C leads to electron accumulation on Fe_3C, and the electron accumulation on Fe_3C can optimize the adsorption/desorption energies of active species to further promote the occurrence of ORR [21,44].

The soybean root derived carbon shows a 3D honeycomb-like structure with multi-channels (Fig. S8), which inherits the structure of soybean root biomass. This 3D honeycomb-like structure is favorable for ions rapid diffusion for ORR. When Co precursor is absent (the ratio of Co to Fe is 0), the obtained product is Fe_3C/HNC, displaying porous structure with some thin carbon nanosheets grown on the substrate (Fig. S9a-b). When an appropriate amount of Co precursor is added (the ratio of Co to Fe is 0.25), the obtained product is Co_3Fe_7-Fe_3C/HNC. The Co_3Fe_7-Fe_3C/HNC displays the 3D porous architecture (Fig. 3a), which inherits the honeycomb-like porous from the biomass soybean root. The magnified SEM image in Fig. 3b shows that numerous carbon nanowires are uniformly distributed in the 3D honeycomb-like N-doped carbon, and the carbon nanowires are interwoven with each other to facilitate electron transfer. When an excessive amount of Co precursor is added (the ratio of Co to Fe is 0.5), the obtained product is Co_3Fe_7/HNC, displaying highly crumpled honeycomb-like structure with some metal particles decorated on carbon substrate (Fig. S9c-d). It is deduced that the ratio of Co to Fe can not only regulate the composition and structure of the final product, but also can modulate the morphology.

Transmission electron microscopy (TEM) image of Co_3Fe_7-Fe_3C/

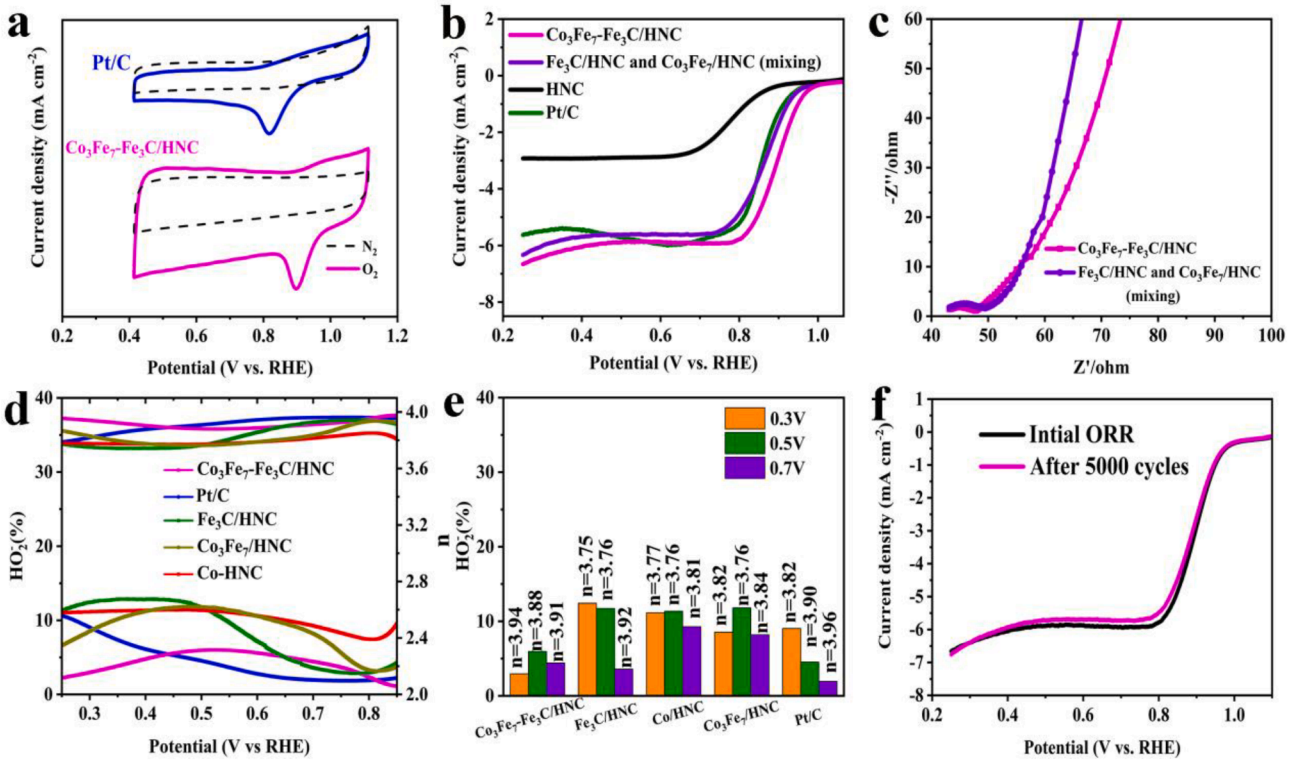

Fig. 4. (a) CV curves of Co_3Fe_7-Fe_3C/HNC and Pt/C in O_2-saturated and N_2-saturated 0.1 M KOH solutions. (b) LSV curves of HNC, the mixture of Co_3Fe_7/HNC and Fe_3C/HNC, Co_3Fe_7-Fe_3C/HNC and Pt/C in O_2-saturated 0.1 M KOH solutions with a scan rate of 10 mV s^{-1} at 1600 rpm. (c) Electrochemical impedance spectroscopy (EIS) spectra for Co_3Fe_7-Fe_3C/HNC and the mixture of Co_3Fe_7/HNC and Fe_3C/HNC. (d, e) Corresponding peroxide yields and electron number. (f) LSV curves of Co_3Fe_7-Fe_3C/HNC before and after 5000th CV cycles at a RDE rotation rate of 1600 rpm in O_2 saturated alkaline solution.

HNC in Fig. 3c shows the thin carbon nanosheet substrate, which are intimately connected with the carbon nanowires. The detailed structure of Co_3Fe_7-Fe_3C is shown in Fig. 3d-e. The Co_3Fe_7 island is trapped by Fe_3C layer, and the interface with distinctly different crystal structures between the two phases of Fe_3C (area 1) and Co_3Fe_7 (area 2) in the catalyst confirms the formation of heterostructure. The corresponding lattice spacing of 0.215 nm and 0.202 nm are assigned to (2 1 1) plane of Fe_3C and (1 1 0) plane of Co_3Fe_7, respectively [45,46]. The corresponding fast Fourier transform (FFT) patterns transformed from the high-resolution transmission electron microscopy (HRTEM) image (Inset in Fig. 3e) also confirms the structure characteristic. In order to better illustrate heterostructure between Co_3Fe_7 and Fe_3C, a colored map created according to the intensity of atoms is shown in Fig. 3f, demonstrating the presence of interface with distinctly crystal structures and electron densities [47,48]. Such an interfacial structure plays a key role in ORR, which will be discussed later. The high angle annular dark-field scanning transmission electron microscope (HAADF-STEM) also confirms the presence of the interface, and the corresponding EDS elemental mappings (Fig. 3g-k) further reveal the uniform distribution of C, N, Fe and Co elements within the matrix. Furthermore, the EDS line-scan elemental profiling in Fig. 3l, m reveals a distinct cross-over between Co and Fe with elemental intensities. By comparing with the intensity of Co and Fe counts near the interface, there is a large amount of Fe atoms in area 1, while the area 2 (island) possesses the elemental distribution of Co and Fe, further indicating the presence of the interfacial structure between Fe_3C and Co_3Fe_7.

The effect of Co_3Fe_7-Fe_3C/HNC on ORR performance was evaluated in 0.1 M KOH electrolyte. Fig. 4a shows the CV curves of Co_3Fe_7-Fe_3C/HNC and Pt/C benchmark at 5 mV s^{-1} in O_2-saturated and N_2-saturated solutions. The obvious cathodic peak is only observed in the O_2-saturated solution, clearly demonstrating the oxygen reduction reaction. Additionally, the reduction peak potential on Co_3Fe_7-Fe_3C/HNC (0.95 V) is more positive than that on Pt/C (0.84 V), demonstrating better electrocatalytic activity. Linear sweep voltammetry (LSV) curves recorded at a rotation speed of 1600 rpm are shown in Fig. S10. The onset potential of Co_3Fe_7-Fe_3C/HNC (0.98 V) is more positive than those on Fe_3C/HNC (0.94 V), Co_3Fe_7/HNC (0.95 V), Co/HNC (0.91 V), HNC (0.90 V) and the benchmark 20 wt% Pt/C (0.98 V), indicating the superior ORR activity. Furthermore, the half-wave potential of Co_3Fe_7-Fe_3C/HNC ($E_{1/2} = 0.90$ V) is more positive than that of 20 wt% Pt/C ($E_{1/2} = 0.85$ V), indicating a smaller energy barrier for ORR. The Co_3Fe_7-Fe_3C/HNC exhibits a larger limiting current density (6.5 mA cm^{-2}) than commercial Pt/C (6.0 mA cm^{-2}). The enhanced ORR performance is mainly ascribed to the interfacial structure at Co_3Fe_7-Fe_3C heterostructure as well as the Co_3Fe_7 and Fe_3C components with desirable properties. Moreover, the corresponding Tafel slope of Co_3Fe_7-Fe_3C/HNC is 85 mV dec^{-1}, which is significantly lower than that of the benchmark Pt/C catalyst (108 mV dec^{-1}) and other reference samples (Fig. S11), indicating bigger charge transfer coefficient.

To demonstrate the essential role of the interfacial structure, the physically mixed sample of Co_3Fe_7/HNC and Fe_3C/HNC without interfacial structure was tested for comparison, and the corresponding LSV curves are shown in Fig. 4b. Clearly, the Co_3Fe_7-Fe_3C/HNC displays better ORR performance than that of the mixture of Co_3Fe_7/HNC and Fe_3C/HNC. Electrochemical impedance spectroscopy (EIS) is shown in Fig. 4c, and the Co_3Fe_7-Fe_3C/HNC shows a lower charge transfer resistance (~4.5 Ω) than that of the control group, demonstrating faster charge transfer kinetics. The enhanced catalytic activity is attributed to the electronic coupling effect arising from the interface between Co_3Fe_7 and Fe_3C, which can boost the electron transfer and enhance the intrinsic electrocatalytic activity [49]. To determine electron transfer number of ORR on Co_3Fe_7-Fe_3C/HNC, LSV curves at various rotating speeds ranging from 400 to 1600 rpm are shown in Fig. S12. The electron transfer number of Co_3Fe_7-Fe_3C/HNC calculated from K-L plots is

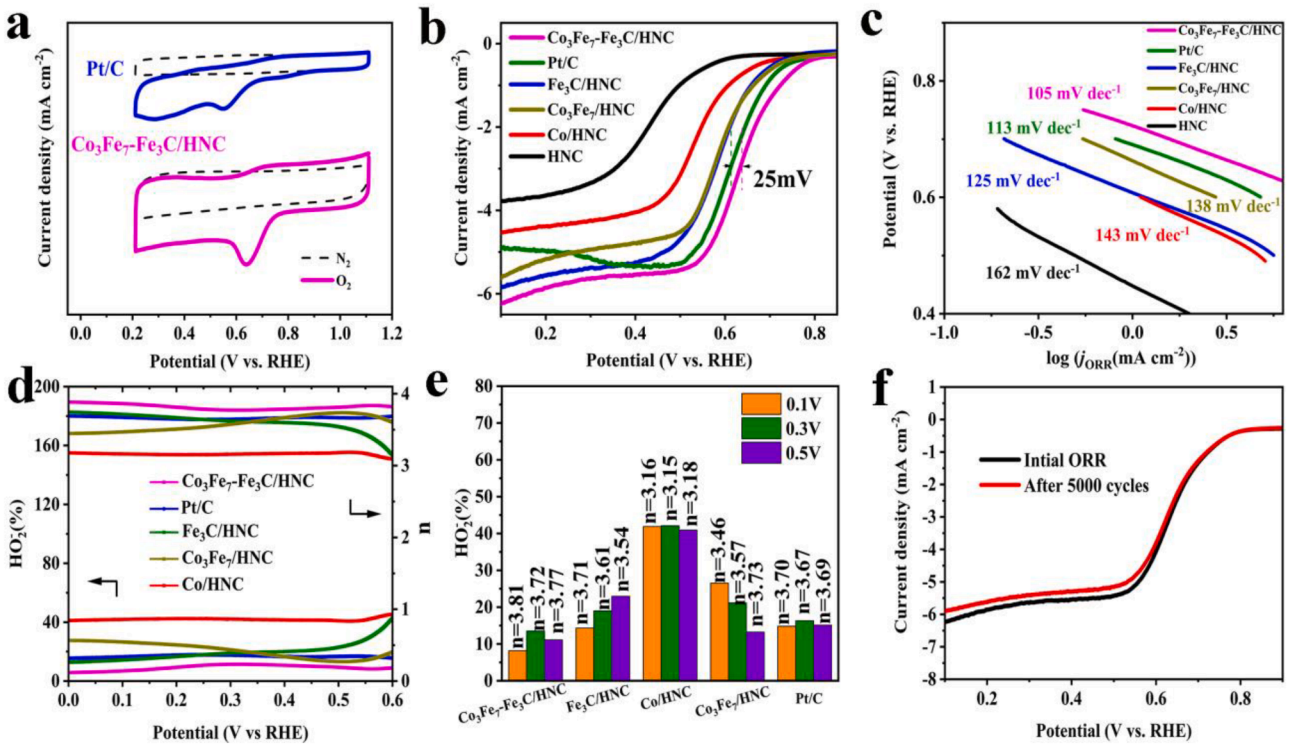

Fig. 5. (a) CV curves of Co_3Fe_7-Fe_3C/HNC and Pt/C in O_2-saturated and N_2-saturated neutral solutions. (b) LSV curves of HNC, Co/HNC, Fe_3C/HNC, Co_3Fe_7/HNC, Co_3Fe_7-Fe_3C/HNC and Pt/C in O_2-saturated neutral solution at a scan rate of 10 mV s^{-1} at 1600 rpm. (c) Tafel slopes curves. (d, e) Corresponding peroxide yields and electron number. (f) LSV curves of Co_3Fe_7-Fe_3C/HNC before and after 5000th CV cycles at a RDE rotation rate of 1600 rpm in O_2 saturated neutral solution.

~4.02 (Inset in Fig. S12), suggesting a direct four-electron pathway. To better clarify electron transfer number and quantify HO_2^- yield, rotating ring disk electrode (RRDE) experiment was performed in 0.1 M KOH solution at a scan rate of 10 mV s^{-1}. From Fig. 4d-e, the Co_3Fe_7-Fe_3C/HNC catalyst shows a low HO_2^- yield of below 10% and a larger electron transfer number of above 3.80, which are close to that of Pt/C catalyst (electron transfer number: 3.84–3.94, H_2O_2 yields: 2.5–8.2%) and better than those of Fe_3C/HNC, Co_3Fe_7/HNC, Co/HNC and HNC. This result indicates the easier access to the desirable four-electron ORR pathway on Co_3Fe_7-Fe_3C/HNC. The stability of Co_3Fe_7-Fe_3C/HNC was evaluated by 5000 consecutive CV cycles, and the ORR polarization curves show that there is no obvious shift of $E_{1/2}$, indicating good durability (Fig. 4f).

ORR performance of Co_3Fe_7-Fe_3C/HNC catalyst was also evaluated in 3.5 wt% NaCl solution. Fig. 5a shows the Co_3Fe_7-Fe_3C/HNC displays a more positive reduction peak potential (0.65 V) than the benchmark Pt/C catalyst (0.55 V), suggesting an effective catalytic activity in the neutral solution. The LSV curves in Fig. 5b show that the Co_3Fe_7-Fe_3C/HNC exhibits an onset potential (E_{onset} = 0.78 V vs. RHE) and a half-wave potential ($E_{1/2}$ = 0.64 V vs. RHE), which are superior to those of commercial Pt/C (E_{onset} = 0.74 V and $E_{1/2}$ = 0.61 V) as well as Fe_3C/HNC, Co_3Fe_7/HNC, Co/HNC and HNC. The corresponding Tafel slope for Co_3Fe_7-Fe_3C/HNC is 105 mV·dec^{-1}, which is lower than that of the benchmark Pt/C catalyst (120 mV dec-1) and other reference samples, suggesting the faster ORR kinetics of Co_3Fe_7-Fe_3C/HNC. Fig. S13 displays the LSV curves at various rotating speeds in O_2-saturated electrolyte and the corresponding K-L plots. The average value of electron transfer is determined to be 3.67, indicating that the Co_3Fe_7-Fe_3C/HNC also undergoes an almost direct four-electron transfer pathway in the neutral solution. Fig. 5d, e show that the calculated H_2O_2 yield on Co_3Fe_7-Fe_3C/HNC is below 25% and the number of electron transfer is 3.70, which is in good agreement with the results of K-L plots. The enhanced activity of Co_3Fe_7-Fe_3C/HNC is explained that the interfacial structure can accelerate ORR kinetics and efficiently boost ORR activity. The Co_3Fe_7-Fe_3C/HNC heterostructure electrocatalyst also shows long-term stability with negligible degradation of $E_{1/2}$ after 5 000 cycles (Fig. 5f), implying the good stability in neutral medium.

To further examine the role of Co_3Fe_7-Fe_3C heterostructure in the hybrid catalyst, the Co_3Fe_7-Fe_3C/HNC was leached in an acid solution to remove partial metallic nanoparticles. The result demonstrates that the leached sample displays a significant activity decay in either alkaline or neutral solutions (Fig. S14a, b), further confirming the effect of Co_3Fe_7-Fe_3C. The electrochemical surface areas (ECSAs) of these materials were further examined from double-layer capacitance (C_{dl}). The C_{dl} of Co_3Fe_7-Fe_3C/HNC, Fe_3C/HNC, Co/HNC and HNC electrodes are 19.74, 15.14, 8.90 and 4.86 mF, respectively (Fig. S15, 16). From HNC to Co_3Fe_7-Fe_3C/HNC, the ECSA increases by 4-fold, demonstrating that Co_3Fe_7-Fe_3C/HNC possesses much more active sites to achieve enhanced ORR catalytic activity.

To predict the possible ORR catalytic mechanism of Co_3Fe_7-Fe_3C/HNC, density functional theory (DFT) calculations were performed. The optimal structure of HNC, Co_3Fe_7/HNC and Co_3Fe_7-Fe_3C/HNC are shown in Fig. 6 and Fig. S17-18. The calculated binding free energies of the reaction intermediates are shown in Tables S1-S3. For the HNC, the binding free energies of OOH*, O* and OH* intermediates are 4.47, 3.24 and 1.71 eV, respectively. For Co_3Fe_7/HNC, the binding free energies of OOH*, O* and OH* are 3.36, 1.72 and 0.47 eV, respectively. The binding free energies of OOH*, O* and OH* intermediates on the Co_3Fe_7-Fe_3C/HNC are 3.41, 2.15 and 1.16 eV, respectively, which are close to that of an ideal catalyst.[50] The diagram of free energy changes for ORR in Fig. 6d shows that all the elementary reactions can occur spontaneously at U = 0 V (zero potential). With the increase in potential, the elementary reaction is less exothermic. Therefore, there exists a limiting potential $U_{limiting}$ (maximum external potential), enables all elementary reactions remain exothermic. When the potential is 1.23 V (equilibrium potential), the elementary reactions are thermodynamically unfavorable. It is seen that the calculated $U_{limiting}$ value for Co_3Fe_7-Fe_3C/HNC is 0.98 V, which is much more positive than that of HNC (0.45 V) and Co_3Fe_7/HNC (0.47 V), suggesting the superior catalytic activity of

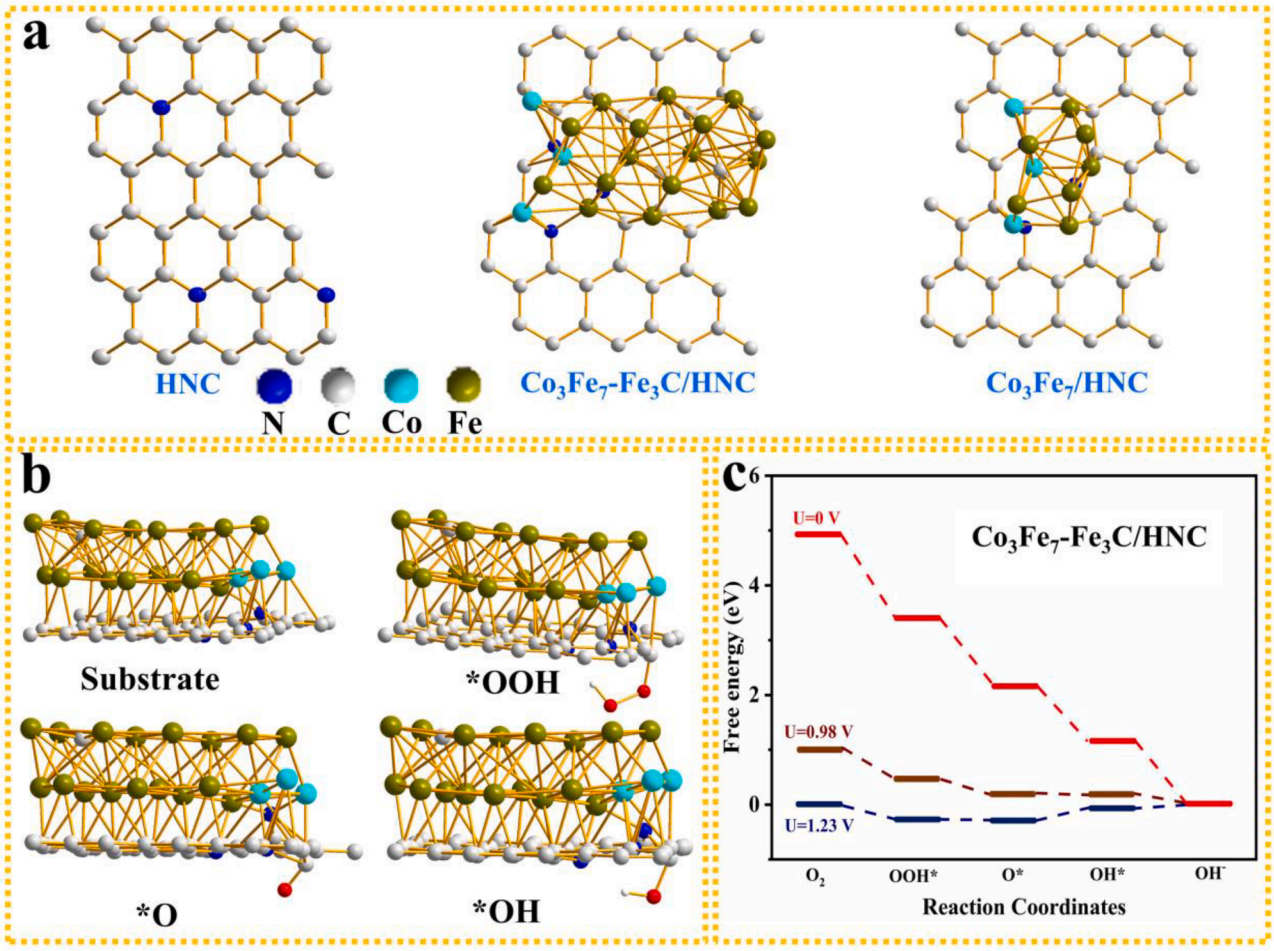

Fig. 6. (a) Top-view schematic models of HNC, Co_3Fe_7/HNC and Co_3Fe_7-Fe_3C/HNC, respectively. (b) Optimized structures of OH*, O*, and OOH* intermediates on Co_3Fe_7-Fe_3C/HNC. (c) Free energy diagram of Co_3Fe_7-Fe_3C/HNC at zero potential ($U = 0$), equilibrium potential ($U = 1.23$ V), and thermodynamic limiting potential.

Co_3Fe_7-Fe_3C/HNC towards ORR. The results suggest that both Co_3Fe_7 and Fe_3C play key roles in ORR.

To explore practical application in both alkaline and neutral solutions, aqueous Al-air batteries based on Co_3Fe_7-Fe_3C/HNC air cathodes were fabricated and evaluated. The discharge curves and corresponding power density curves of the Al-air batteries based on Co_3Fe_7-Fe_3C/HNC and Pt/C are shown in Fig. 7a. The maximum power density of the Al-air battery based on Co_3Fe_7-Fe_3C/HNC is 210 mW cm^{-2} at a current density of 286 mA cm^{-2}, which is 1.2 times as that of Pt/C (180 mW cm^{-2} at a current density of 273 mA cm^{-2}). The Al-air battery based on Co_3Fe_7-Fe_3C/HNC displays stable working voltages of ~1.58 V and ~ 1.21 V at current densities of 20 and 100 mA cm^{-2}, respectively, which are also larger than those of Pt/C at both current densities (Fig. 7b). To show the potential application for practical devices, two alkaline Al-air batteries connected in series are demonstrated to marvelously charge a mobile phone (Fig. 7c). Neutral electrolyte is more environmental benignity. Therefore, Al-air batteries in neutral electrolytes are great of interest. As shown in Fig. 7d, the maximum power density of the Al-air battery based on Co_3Fe_7-Fe_3C/HNC in a NaCl solution is 20.94 mW cm^{-2}, which is superior to that of the commercial Pt/C. Fig. 7e displays the discharge curves at current densities of 5 and 20 mA cm^{-2}. The working voltage of the neutral Al-air battery based on Co_3Fe_7-Fe_3C/HNC is also larger than that based on 20% Pt/C. As a demonstration, two neutral Al–air batteries connected in series can effectively power 65 LEDs with "SJTU" shape (Fig. 7f). Although it is a primary battery, it can be mechanically recharged to realize continuous discharge with nearly no voltage decay (Fig. 7g). The Al anode is oxidized and gradually consumed during discharge. Once the Al anode is completed, the discharge ceases. Then a new Al anode is mechanically refilled in the cell, and the Al-air battery can discharge again. In order to further confirm the stability of the air cathode, the Al-air battery based on the Co_3Fe_7-Fe_3C/HNC can continue to discharge for 70 h at 100 mA cm^{-2} (Fig. 7h).

4. Conclusions

In summary, the Co_3Fe_7-Fe_3C/HNC derived from biomass has been fabricated via an interfacial engineering strategy. Benefiting from the unique 3D honeycomb-like structure inherited from the biomass and the interfacial structure between Fe_3C and Co_3Fe_7, the Co_3Fe_7-Fe_3C/HNC catalyst exhibits superior electrocatalytic activities towards ORR, which is supported by DFT calculation. The interfacial structure between Co_3Fe_7 and Fe_3C can accelerate charge transfer to boost electrochemical activity for ORR. The fabricated Al-air batteries based on Co_3Fe_7-Fe_3C/HNC catalyst demonstrate remarkable discharge performance. This work presents a new avenue to explore the design of multifunctional catalysts with interfacial structure for high performance metal-air batteries.

Declaration of Competing Interest

The authors declare that they have no known competing financial interests or personal relationships that could have appeared to influence the work reported in this paper.

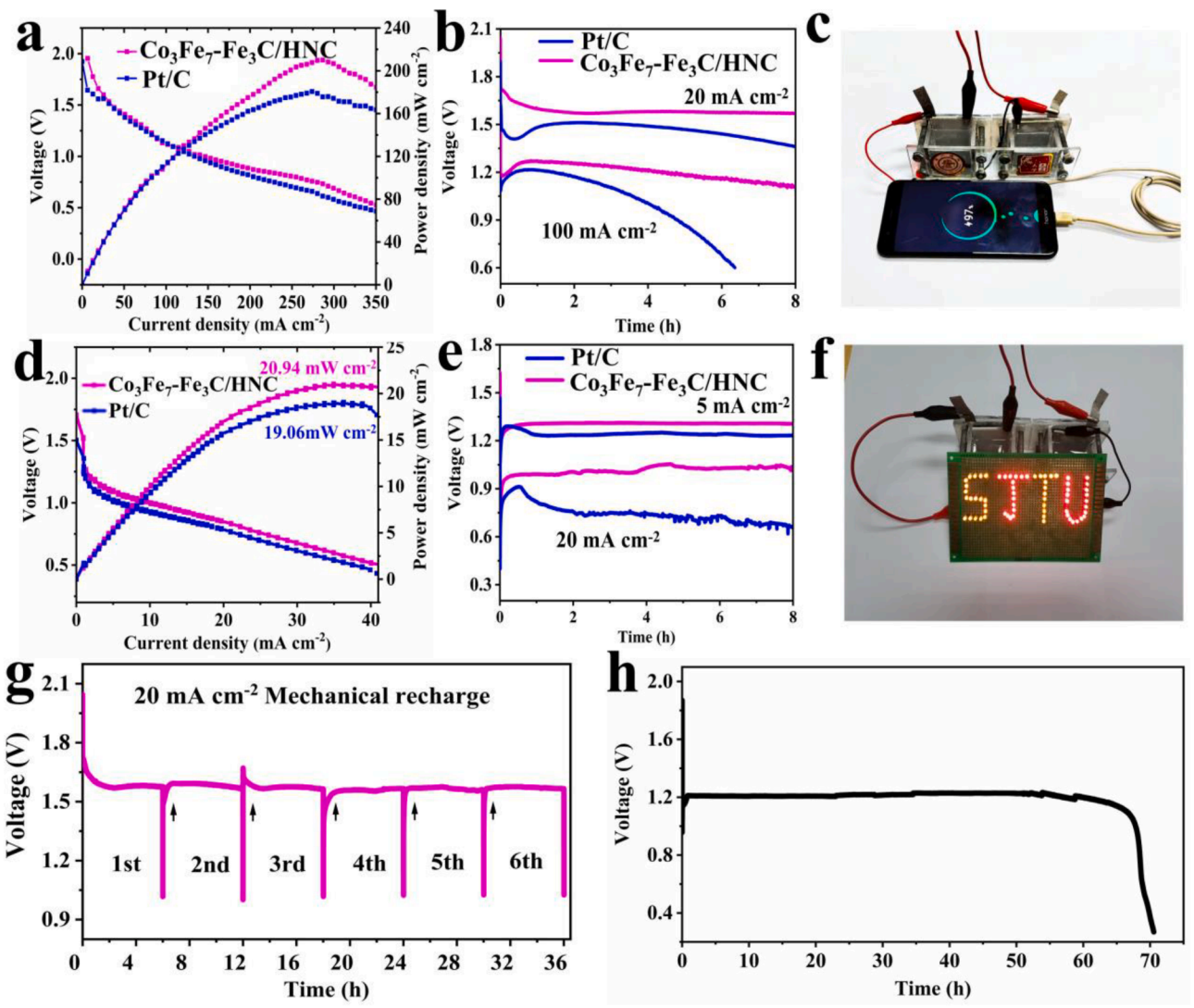

Fig. 7. (a) Discharge polarization curve and the corresponding power plots of the alkaline Al-air batteries using Co_3Fe_7-Fe_3C/HNC and 20% Pt/C catalysts. (b) Galvanostatic discharge curves at current densities of 20 and 100 mA cm^{-2}. (c) The home-made Al-air batteries in four series powered a mobile phone. (d) Discharge polarization curve and the corresponding power plots under neutral solution. (e) Galvanostatic discharge curves at current densities of 5 and 20 mA cm^{-2}. (f) The neutral Al-air batteries in two series powered 65 LEDs with "SJTU" shape. (g) The alternatively mechanical recharge of the Al-air batteries under alkaline solution (h) Mechanical charge and discharge tests using the Co_3Fe_7-Fe_3C/HNC at 100 mA cm^{-2}.

Acknowledgments

This work was supported by the National Natural Science Foundation of China (51874197, 51704106). The authors gratefully acknowledge the facilities and technical assistance at Instrumental Analysis Center of SJTU.

Appendix A. Supplementary data

Supplementary data to this article can be found online at https://doi.org/10.1016/j.cej.2020.127124.

References

[1] S. Chu, A. Majumdar, Opportunities and challenges for a sustainable energy future, Nature 488 (7411) (2012) 294–303.
[2] V.R. Stamenkovic, D. Strmcnik, P.P. Lopes, N.M. Markovic, Energy and fuels from electrochemical interfaces, Nat. Mater 16 (1) (2017) 57–69.
[3] D.U. Lee, J.-Y. Choi, K. Feng, H.W. Park, Z. Chen, Advanced extremely durable 3D bifunctional air electrodes for rechargeable zinc-air batteries, Adv. Energy Mater. 4 (2014) 1301389.
[4] Y. Li, M. Gong, Y. Liang, J. Feng, J.-E. Kim, H. Wang, G. Hong, B. Zhang, H. Dai, Advanced zinc-air batteries based on high-performance hybrid electrocatalysts, Nat. Commun. 4 (2013) 1805.
[5] H.-J. Qiu, P. Du, K. Hu, J. Gao, H. Li, P. Liu, T. Ina, K. Ohara, Y. Ito, M. Chen, Metal and nonmetal codoped 3D nanoporous graphene for efficient bifunctional electrocatalysis and rechargeable Zn–Air batteries, Adv. Mater. 31 (2019) 1900843.
[6] X.F. Lu, Y. Chen, S. Wang, S. Gao, X.W. Lou, Interfacing manganese oxide and cobalt in porous graphitic carbon polyhedrons boosts oxygen electrocatalysis for Zn–Air batteries, Adv. Mater. 31 (2019) 1902339.
[7] G. Nam, Y. Son, S.O. Park, W.C. Jeon, H. Jang, J. Park, S. Chae, Y. Yoo, J. Ryu, M. G. Kim, S.K. Kwak, J. Cho, A ternary $Ni_{46}Co_{40}Fe_{14}$ nanoalloy-based oxygen electrocatalyst for highly efficient rechargeable zinc-air batteries, Adv. Mater. 30 (2018) 1803372.
[8] C.C. Yang, S.F. Zai, Y.T. Zhou, L. Du, Q. Jiang, Fe_3C-Co nanoparticles encapsulated in a hierarchical structure of N-doped carbon as a multifunctional electrocatalyst for ORR, OER, and HER, Adv. Funct. Mater. 29 (2019) 1901949.
[9] S. Sultan, J.N. Tiwari, J.-H. Jang, A.M. Harzandi, F. Salehnia, S.J. Yoo, K.S. Kim, Highly efficient oxygen reduction reaction activity of graphitic tube encapsulating Nitrided Co_xFe_y alloy, Adv. Energy Mater. 8 (2018) 1801002.
[10] M. Jiang, C. Fu, J. Yang, Q.i. Liu, J. Zhang, B. Sun, Defect-engineered MnO_2 enhancing oxygen reduction reaction for high performance Al-air batteries, Energy Storage Mater. 18 (2019) 34–42.
[11] Y. Yuan, J. Wang, S. Adimi, H. Shen, T. Thomas, R. Ma, J.P. Attfield, M. Yang, Zirconium nitride catalysts surpass platinum for oxygen reduction, Nat. Mater. 19 (3) (2020) 282–286.

[12] A.A. Eissa, S.G. Peera, N.H. Kim, J.H. Lee, g-C 3 N 4 templated synthesis of the Fe 3 C@NSC electrocatalyst enriched with Fe–N x active sites for efficient oxygen reduction reaction, J. Mater. Chem. A 7 (28) (2019) 16920–16936.

[13] G. Fu, Y. Chen, Z. Cui, Y. Li, W. Zhou, S. Xin, Y. Tang, J.B. Goodenough, Novel hydrogel-derived bifunctional oxygen electrocatalyst for rechargeable air cathodes, Nano Lett. 16 (10) (2016) 6516–6522.

[14] X. Liu, M. Park, M.G. Kim, S. Gupta, G. Wu, J. Cho, Integrating NiCo alloys with their oxides as efficient bifunctional cathode catalysts for rechargeable zinc-air batteries, Angew. Chem. Int. Ed. 54 (33) (2015) 9654–9658.

[15] M. Jiang, J. Yang, J. Ju, W. Zhang, L. He, J. Zhang, C. Fu, B. Sun, Space-confined synthesis of CoNi nanoalloy in N-doped porous carbon frameworks as efficient oxygen reduction catalyst for neutral and alkaline aluminum-air batteries, Energy Storage Mater. 27 (2020) 96–108.

[16] Y.-Y. Ma, Z.-L. Lang, L.-K. Yan, Y.-H. Wang, H.-Q. Tan, K. Feng, Y.-J. Xia, J. Zhong, Y. Liu, Z.-H. Kang, Y.-G. Li, Highly efficient hydrogen evolution triggered by a multi-interfacial Ni/WC hybrid electrocatalyst, Energy Environ. Sci. 11 (8) (2018) 2114–2123.

[17] Y. Ji, H. Dong, C. Liu, Y. Li, The progress of metal-free catalysts for the oxygen reduction reaction based on theoretical simulations, J. Mater. Chem. A 6 (28) (2018) 13489–13508.

[18] C. Li, M. Wu, R. Liu, High-performance bifunctional oxygen electrocatalysts for zinc-air batteries over mesoporous Fe/Co-N-C nanofibers with embedding FeCo alloy nanoparticles, Appl. Catal. B 244 (2019) 150–158.

[19] H. Li, C. Chen, D. Yan, Y. Wang, R.u. Chen, Y. Zou, S. Wang, Interfacial effects in supported catalysts for electrocatalysis, J. Mater. Chem. A 7 (41) (2019) 23432–23450.

[20] Y. Lin, L. Yang, Y. Zhang, H. Jiang, Z. Xiao, C. Wu, G. Zhang, J. Jiang, L. Song, Defective carbon–CoP nanoparticles hybrids with interfacial charges polarization for efficient bifunctional oxygen electrocatalysis, Adv. Energy Mater. 8 (2018) 1703623.

[21] Z. Xue, X. Li, Q. Liu, M. Cai, K. Liu, M. Liu, Z. Ke, X. Liu, G. Li, Interfacial electronic structure modulation of NiTe Nanoarrays with NiS nanodots facilitates electrocatalytic oxygen evolution, Adv. Mater. 31 (2019) 1900430.

[22] Q. Liang, L. Zhong, C. Du, Y. Luo, J. Zhao, Y. Zheng, J. Xu, J. Ma, C. Liu, S. Li, Q. Yan, Interfacing epitaxial dinickel phosphide to 2D nickel thiophosphate nanosheets for boosting electrocatalytic water splitting, ACS Nano 13 (7) (2019) 7975–7984.

[23] Y. Yang, Y. Wang, H.-L. He, W. Yan, L.. Fang, Y.-B. Zhang, Y. Qin, R. Long, X.-M. Zhang, X. Fan, Covalently connected Nb4N5–xOx–MoS2 heterocatalysts with desired electron density to boost hydrogen evolution, ACS Nano 14 (4) (2020) 4925–4937.

[24] R. Liang, C. Shu, A. Hu, M. Li, Z. Ran, R. Zheng, J. Long, Interface engineering induced selenide lattice distortion boosting catalytic activity of heterogeneous $CoSe_2$@$NiSe_2$ for lithium-oxygen battery, Chem. Eng. J 393 (2020), 124592.

[25] J. Diao, Y. Qiu, S. Liu, W. Wang, K. Chen, H. Li, W. Yuan, Y. Qu, X. Guo, Interfacial engineering of W_2N/WC heterostructures derived from solid-state synthesis: a highly efficient trifunctional electrocatalyst for ORR, OER, and HER, Adv. Mater. 32 (2020) 1905679.

[26] X. Zheng, X. Han, Y. Cao, Y. Zhang, D. Nordlund, J. Wang, S. Chou, H. Liu, L. Li, C. Zhong, Y. Deng, W. Hu, Identifying dense $NiSe_2$/$CoSe_2$ heterointerfaces coupled with surface high-valence bimetallic sites for synergistically enhanced oxygen electrocatalysis, Adv. Mater. 32 (26) (2020) 2000607.

[27] J. Lai, B. Huang, Y. Tang, F. Lin, P. Zhou, X.u. Chen, Y. Sun, F. Lv, S. Guo, Barrier-free interface electron transfer on PtFe-Fe_2C janus-like nanoparticles boosts oxygen catalysis, Chem 4 (5) (2018) 1153–1166.

[28] H. Wang, F.-X. Yin, N. Liu, R.-H. Kou, X.-B. He, C.-J. Sun, B.-H. Chen, D.-J. Liu, H.-Q. Yin, Engineering Fe–Fe_3C@Fe–N–C active sites and hybrid structures from dual metal-organic frameworks for oxygen reduction reaction in H_2–O_2 fuel cell and Li–O_2 battery, Adv. Funct. Mater. 29 (2019) 1901531.

[29] M.R. Lukatskaya, O. Mashtalir, C.E. Ren, Y. Dall'Agnese, P. Rozier, P.L. Taberna, M. Naguib, P. Simon, M.W. Barsoum, Y. Gogotsi, Cation intercalation and high volumetric capacitance of two-dimensional titanium carbide, Science 341 (2013) 1502.

[30] S.J. Clark, M.D. Segall, C.J. Pickard, P.J. Hasnip, M.I. Probert, K. Refson, M. C. Payne, First principles methods using CASTEP, Z. Kristallogr. 220 (2005) 567–570.

[31] E.R. McNellis, J. Meyer, K. Reuter, Azobenzene at coinage metal surfaces: role of dispersive van der Waals interactions, Phys. Rev. B 80 (2009), 205414.

[32] N. Guo, W. Luo, R. Guo, D. Qiu, Z. Zhao, L. Wang, D. Jia, J. Guo, Interconnected and hierarchical porous carbon derived from soybean root for ultrahigh rate supercapacitors, J. Alloys Compd. 834 (2020), 155115.

[33] J. Deng, L. Yu, D. Deng, X. Chen, F. Yang, X. Bao, Highly active reduction of oxygen on a FeCo alloy catalyst encapsulated in pod-like carbon nanotubes with fewer walls, J. Mater. Chem. A 1 (47) (2013) 14868.

[34] J. Liang, Y. Jiao, M. Jaroniec, S.Z. Qiao, Sulfur and nitrogen dual-doped mesoporous graphene electrocatalyst for oxygen reduction with synergistically enhanced performance, Angew. Chem. Int. Ed. 51 (46) (2012) 11496–11500.

[35] H.-K. Jeong, Y.P. Lee, R.J.W.E. Lahaye, M.-H. Park, K.H. An, I.J. Kim, C.-W. Yang, C.Y. Park, R.S. Ruoff, Y.H. Lee, Evidence of graphitic AB stacking order of graphite oxides, J. Am. Chem. Soc. 130 (2008) 1362–1366.

[36] Z.-H. Sheng, L. Shao, J.-J. Chen, W.-J. Bao, F.-B. Wang, X.-H. Xia, Catalyst-free synthesis of nitrogen-doped graphene via thermal annealing graphite oxide with melamine and its excellent electrocatalysis, ACS Nano 5 (6) (2011) 4350–4358.

[37] S. Gao, K. Geng, H. Liu, X. Wei, M. Zhang, P. Wang, J. Wang, Transforming organic-rich amaranthus waste into nitrogen-doped carbon with superior performance of the oxygen reduction reaction, Energy Environ. Sci. 8 (1) (2015) 221–229.

[38] Z. Wang, S. Peng, Y. Hu, L. Li, T. Yan, G. Yang, D. Ji, M. Srinivasan, Z. Pan, S. Ramakrishna, Cobalt nanoparticles encapsulated in carbon nanotube-grafted nitrogen and sulfur co-doped multichannel carbon fibers as efficient bifunctional oxygen electrocatalysts, J. Mater. Chem. A 5 (10) (2017) 4949–4961.

[39] K. Niu, B. Yang, J. Cui, J. Jin, X. Fu, Q. Zhao, J. Zhang, Graphene-based non-noble-metal Co/N/C catalyst for oxygen reduction reaction in alkaline solution, J. Power Sources 243 (2013) 65–71.

[40] G. Tao, L. Zhang, L. Chen, X. Cui, Z. Hua, M. Wang, J. Wang, Y. Chen, J. Shi, N-doped hierarchically macro/mesoporous carbon with excellent electrocatalytic activity and durability for oxygen reduction reaction, Carbon 86 (2015) 108–117.

[41] A. Aijaz, J. Masa, C. Rösler, W. Xia, P. Weide, A.J.R. Botz, R.A. Fischer, W. Schuhmann, M. Muhler, Co@Co3O4 encapsulated in carbon nanotube-grafted nitrogen-doped carbon polyhedra as an advanced bifunctional oxygen electrode, Angew. Chem. Int. Ed. 55 (12) (2016) 4087–4091.

[42] Ling Lin, Qing Zhu, An-Wu Xu, Noble-metal-free Fe–N/C catalyst for highly efficient oxygen reduction reaction under both alkaline and acidic conditions, J. Am. Chem. Soc. 136 (31) (2014) 11027–11033.

[43] S. Maldonado, K.J. Stevenson, Direct Preparation Of Carbon Nanofiber Electrodes Via Pyrolysis Of iron(II) phthalocyanine: electrocatalytic aspects for oxygen reduction, J. Physical Chem. B 108 (2004) 11375–11383.

[44] G. Yang, Y. Jiao, H. Yan, Y. Xie, A. Wu, X. Dong, D. Guo, C. Tian, H. Fu, Interfacial engineering of MoO2-FeP heterojunction for highly efficient hydrogen evolution coupled with biomass electrooxidation, Adv. Mater. 32 (2020) 2000455.

[45] X. Zhao, X. Nie, Y. Li, Y. Pu, X. Sun, R. Yu, X. Liu, J. Shui, A layered double hydroxide-derived exchange spring magnet array grown on graphene and its application as an ultrathin electromagnetic wave absorbing material, J. Mater. Chem. C 7 (39) (2019) 12270–12277.

[46] P. Zhao, X. Hua, W. Xu, W. Luo, S. Chen, G. Cheng, Metal–organic framework-derived hybrid of Fe 3 C nanorod-encapsulated, N-doped CNTs on porous carbon sheets for highly efficient oxygen reduction and water oxidation, Catal. Sci. Technol. 6 (16) (2016) 6365–6371.

[47] B.H.R. Suryanto, Y. Wang, R.K. Hocking, W. Adamson, C. Zhao, Overall electrochemical splitting of water at the heterogeneous interface of nickel and iron oxide, Nature Commun. 10 (2019) 5599.

[48] J. Li, Y. Wang, T. Zhou, H. Zhang, X. Sun, J. Tang, L. Zhang, A.M. Al-Enizi, Z. Yang, G. Zheng, Nanoparticle superlattices as efficient bifunctional electrocatalysts for water splitting, J. Am. Chem. Soc. 137 (45) (2015) 14305–14312.

[49] F. Song, W. Li, J. Yang, G. Han, P. Liao, Y. Sun, Interfacing nickel nitride and nickel boosts both electrocatalytic hydrogen evolution and oxidation reactions, Nature Commun. 9 (2018) 4531.

[50] J.K. Nørskov, J. Rossmeisl, A. Logadottir, L. Lindqvist, J.R. Kitchin, T. Bligaard, H. Jónsson, Origin of the overpotential for oxygen reduction at a fuel-cell cathode, J. Phys. Chem. B 108 (46) (2004) 17886–17892.